

Observation of Nonlinear Shear Wave Propagation Using Magnetic Resonance Elastography

Ingolf Sack,^{1*} Christopher K. McGowan,² Abbas Samani,³ Chris Luginbuhl,³ Wendy Oakden,² and Donald B. Plewes³

MR elastography (MRE) is an MRI modality that is increasingly being used to image tissue elasticity throughout the body. One MRE technique that has received a great deal of attention is based on visualizing shear waves, which reveal stiffness by virtue of their local wavelength. However, the shape of propagating shear waves can also provide valuable information about the nonlinear stress-strain behavior of tissue. Here an experiment is proposed that allows the observation of nonlinear wave propagation based on spatial-temporal phase contrast images. A theoretical description of the wave propagation was developed that reflects typical MRE excitation, which involves excitation modes both parallel and perpendicular to B_0 . Based on this model, it is shown that both odd and even higher harmonics are produced with their amplitudes dependent on the details of the actuator, imaging geometry, and the nonlinear tissue properties. With appropriate motion encoding, harmonic vibrations arising from nonlinear tissue response can be detected. The effect is demonstrated on an agarose gel phantom using a sinusoidal shear vibration of 150 Hz, and clearly shows the presence of harmonics at 600 and 750 Hz. Using an estimate of the strain energy of the phantom, we were able to determine the nonlinear tissue properties. Magn Reson Med 52: 842–850, 2004. © 2004 Wiley-Liss, Inc.

Key words: nonlinear wave propagation; MR elastography; shear waves; nonlinear harmonics; anharmonic vibrations

In recent years, MR elastography (MRE) has received considerable interest as a novel modality that is capable of imaging tissue elasticity *in vivo*. Originally based on ultrasound (US) imaging, elastography applications in MRI have made rapid progress. The highly-resolved soft-tissue contrast gained by MRI, combined with the shear modulus as a sensitive elasticity parameter, have led several investigators to employ MRE in a number of clinical applications, including the prostate (1,2), head (3–6), skeletal muscle (7–9), and breast (10–12). MRE is based on the detection of spin phase contrast arising from oscillatory motion in the presence of phase-locked magnetic field gradients (13). This allows the propagation of acoustic shear waves to be imaged along the direction of the applied motion-encoding gradients. To date, tissue stiffness has been examined in MRE in terms of the shear modulus μ as a linear elastic material property. The linear shear

modulus can be analyzed by means of local wave speeds based on local frequency estimators (14,15), from inverse solutions of the Navier equations (11,16), or an iterative refinement of displacements (17,18). However, using real-time US, Catheline et al. (19–21) recently demonstrated that low-frequency (100 Hz) transverse waves can exhibit nonlinear propagation effects while traveling through agarose gel. Although such thermo-reversible gels have been found to be linear elastic under small static deformations, shear waves cause third-order nonlinear effects due to the high particle deflection speed relative to the low shear wave propagation speed. One can visualize the nonlinear effects by creating higher harmonic frequency components of the fundamental shear vibration, whose intensity ratios, shock speeds, and total amplitudes are sensitive to both applied strain components and the inherent nonlinear stress-strain function of the material (22). These nonlinear parameters may provide new information regarding tissue type, as previous rheologic experiments have shown that most tissues exhibit nonlinear constitutive properties (23). The goal of this study was to introduce a methodology that exploits the potential of MRE in demonstrating these nonlinear properties in an imaging experiment.

BACKGROUND

Temporal Resolution of MRE

In contrast to real-time US observation of nonlinear transverse waves (20), MRE acquires data by phase encoding each line in k -space with appropriate oscillatory motion-encoding gradients. Through the use of sinusoidal motion-encoding gradients, the final image selectively shows oscillatory wave motions, which occur with a frequency content that is dependent on the details of the gradient. Ideally, an MRE experiment would not be limited by tissue T_2 , and hence long motion-encoding gradients could be applied. This would result in an image that would be selective only for motions that occur at the frequency of the gradient. However, due to the short T_2 times of tissues, these gradients are short (on the order of 10–200 ms), which broadens the spectral response of any practical MRE experiment. As such, MRE gradients serve to operate as a filter by which the spectral response of tissue motions will be scaled depending on the details of gradient encoding.

The resultant phase image reports the spatial distribution of motion, and the gradients act in a stroboscopic manner to capture the tissue motions. To achieve a time-resolved rendering of the shear wave progression, repetitive MRE acquisitions are required while the phase φ is incremented between the motion and gradient waveforms. As such, the time required to achieve time-resolved 2D

¹Institute of Radiology, Charité-University Medicine Berlin, Humboldt University Berlin, Berlin, Germany.

²Department of Medical Imaging, Hospital for Sick Children, University of Toronto, Toronto, Ontario, Canada.

³Imaging Research, Sunnybrook and Women's College Health Sciences Centre, University of Toronto, Toronto, Canada.

*Correspondence to: Ingolf Sack, Ph.D., Institute of Radiology, Charité-University Medicine Berlin, Humboldt, University Berlin, Schumannstr. 20/21, 10117 Berlin, Germany. E-mail: ingolf.sack@charite.de

Received 10 October 2003; revised 1 June 2004; accepted 1 June 2004.

DOI 10.1002/mrm.20238

Published online in Wiley InterScience (www.interscience.wiley.com).

MRE data can be lengthy. For application to linear shear wave propagation, this may require a minimum of four increments of φ to adequately capture the temporal evolution of the wave propagation. However, for application to nonlinear wave propagation, many more phase increments will be needed to track the evolution of higher harmonics depending on the order of the harmonics under investigation. As such, the time required to complete a full investigation of nonlinear effects in MRE can be prohibitive. An alternative approach is to sacrifice one spatial dimension of encoding while increasing the temporal resolution by using a 1D spatial imaging method, and automatically incrementing the phase φ between the motion and gradient applications (24). This approach will balance the need to provide high temporal resolution for monitoring higher harmonics while providing the needed spatial rendering to appreciate the spatial evolution of nonlinear effects.

MRE Tissue Excitation

The nature of the harmonic generation arising from nonlinear effects depends on the nature of the possible motions that can occur in tissue. Catheline et al. (19) have shown that nonlinear mechanisms coupled from purely longitudinal waves will generate even-order harmonics while the same nonlinear mechanisms arising from transverse wave motion will generate odd-order harmonics. As such, in order to appreciate the order of harmonic generation, it is important to appreciate the details of the mechanical excitation in terms of motion components that are parallel and perpendicular to the image axis of the shear waves.

In the case of MRE, shear wave excitation is commonly achieved with the use of electromechanical actuator systems (13). Typically, such systems use an “excitation” coil mounted on a gimbaled beam with the opposite end attached to the patient surface over an “actuator surface.” With the application of an alternating current to this coil, the resulting interaction with the static magnet field will create an alternating torque on the coil parallel to \bar{B}_0 . The induced vibrations of the induction coil are carried forward via beam and transducer plate to the phantom surface. The type of connection between the actuator and the object determines the shape of the induced shear waves. In our experiments, the transducer plate was chosen to flatly cover the whole surface of the agarose phantom in order to ensure a creation of only parallel transverse waves. However, it is important to note that the actuator is not necessarily aligned with the coordinate system of the scanner. As shown in Fig. 1, a minor tilt of the actuator system (labeled as X' and Y') relative to the B_0 -axis would yield an observable fraction of $u_x(x, y)$ displacement, which is not present if X' and X coincide. Thus, the measured displacement reflects only the projection of the motion vector onto the coordinate axis that is chosen by the direction of the oscillating gradients. For an analysis of the nonlinear strain elements, the spatial dependency of the true motion vector must be taken into account.

In the next section, we develop a brief theoretical description of the spectral response of MRE, followed by a model of nonlinear wave propagation for this type of excitation. Finally, we demonstrate these effects using a 1D

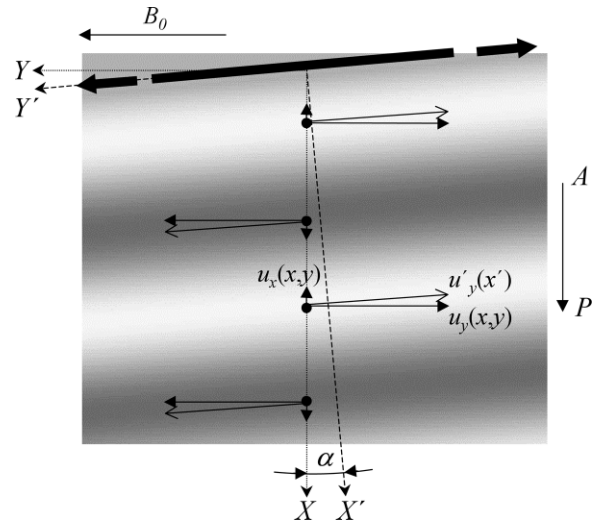


FIG. 1. The vibration vectors induced by the actuator (parallel to Y') and their decompositions into the motion components, as they would be detected by MRE. The oscillating gradients of the MRE sequence are aligned with B_0 so that the y -component of the deflection u is encoded.

MRE pulse sequence in an experimental system based on a simple agar phantom.

THEORY

MRE Spectral Response

We will first consider the displacement of a particle without specific direction at an arbitrary location. The time dependency of the deflection is given as a harmonic function:

$$u(t) = A_v \sin(2\pi f_v t + \theta). \quad [1]$$

where f_v is the frequency, A_v is the amplitude of the tissue vibrations, and θ refers to the spatial phase of the oscillations at that given point. This phase depends on the speed of the shear wave through the material, and the initial phase φ of the excitation with respect to the gradient and the vibration frequency f_v . For linear elasticity, f_v is simply equal to the experimental driving frequency (f_0). In the case of nonlinear wave propagation, multiple values of f_v will be present in the sample. The displacement $u(t)$ of the particle is detected in MRE in terms of a phase shift ϕ , which is imposed by an oscillating gradient of frequency f_G and amplitude A_G :

$$\phi = \int_0^\tau \gamma A_G \sin(2\pi f_G t) \cdot u(t) dt, \quad [2]$$

where γ is the gyromagnetic ratio of the proton spins, and τ refers to the duration of the encoding gradient characterized by $\tau = n_G/f_G$, with n_G as the number of gradient periods. The number of gradient cycles n_G is limited to a

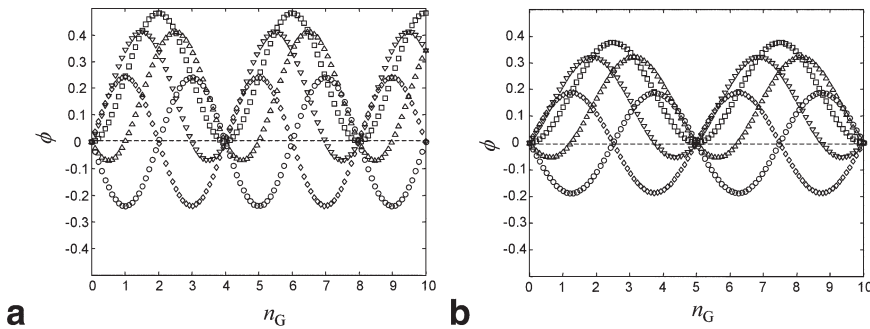


FIG. 2. Functions of the encoding signal ϕ (Eq. [3]) vs. gradient periods n_G for $f_v = 150$ Hz, $f_G = 600$ Hz (a), and $f_G = 750$ Hz (b). The spatial phase was varied as $\theta(x,y) = 0$ (\circ), $\theta(x,y) = \pi/4$ (\triangle), $\theta(x,y) = \pi/2$ (\square), $\theta(x,y) = 3\pi/4$ (∇), and $\theta(x,y) = \pi$ (\diamond). For the simulations, a gradient amplitude of 40 mT/m and a vibration amplitude of ± 0.5 mm were assumed.

certain number of approximately 10–30 due to T_2^* relaxation processes. Therefore, the finite bandwidth of the gradient may cause an encoding of frequency components that differ from the gradients frequency. Under the assumption of an integer n_G , the solution of the integral in Eq. [2] using Eq. [1] follows for the case of $f_G \neq f_v$:

$$\phi = \gamma A_G A_v \frac{f_G}{\pi(f_v^2 - f_G^2)} \times (\sin \theta \cos^2 \Omega - \sin \theta + \cos \theta \sin \Omega \cos \Omega), \quad [3]$$

with

$$\Omega = \frac{\pi f_v n_G}{f_G}. \quad [4]$$

For the resonance condition $f_G = f_v$, the integral of Eq. [2] yields the well-known relation:

$$\phi = \frac{1}{2} \frac{\gamma A_G A_v n_G}{f_v} \cos \theta. \quad [5]$$

From this equation, it follows that the magnitude of the encoded signal ϕ increases linearly with the number of gradient periods for positions where $\cos \theta \neq 0$. In contrast, for $f_G \neq f_v$, a phase will remain that is determined by the ratio of both frequencies and the number of gradient cycles n_G . Alternatively, if the number of gradient cycles fulfills the relation

$$n_G = \frac{f_G}{f_v} n; \quad n = 1, 2, 3, \dots \quad [6]$$

then only the selected harmonic f_v is encoded, while all multiples of the vibration frequency exhibit null phase amplitude. For example, the application of a 600-Hz gradient frequency would remove all 150-Hz components with $n_G = 4, 8, \dots$ (see Fig. 2a).

Nonlinear Shear Wave Propagation

In the proposed 1D MRE technique, 1D spatial resolution of the transverse displacement component is considered. Therefore, we introduce \mathbf{u} as a two-component vector that consists of the displacements along the X - and Y -axes of

the imaging coordinate system (Y is parallel to the field, while X is orthogonal). Assuming a pure shear displacement along Y , \mathbf{u} is only a function of position x . However, in MRE experiments, a strict alignment of the coordinate of the spin phase encoding with the deflection axis of the actuator beam is not guaranteed. Therefore, \mathbf{u} becomes dependent on x and y , whereby the displacement component $u_x(x, y)$ can be related to $u_y(x, y)$ if the transformation from the actuator to the scanner system is known. A tilt of the actuator system around the normal of the X - Y plane would influence the ratio of $u_x(x, y)$ and $u_y(x, y)$, as demonstrated in Fig. 1. The tilt angle α is introduced to correlate the two motion components, and \mathbf{u} follows with

$$\mathbf{u} = [\zeta u_y(x, y), u_y(x, y)], \quad [7]$$

for $\zeta = \tan \alpha$. As explained in more detail in the Appendix, it is now possible to derive the deformation of an incompressible medium in terms of the transversal deformation $F = \partial u_y / \partial x$ (the position dependency of $u_y(x, y)$ is henceforth not explicitly stated). In the proposed nonlinear MRE experiment, the deflection u_y is measured along X , and thus the deformation F is an experimentally known quantity. The nonlinear elastic modulus that governs the response of the material to the applied stresses is expressed as a function of F with

$$E = 3E_1 F^2 - 2E_2 F + \mu, \quad [8]$$

The coefficients E_1 and E_2 are derived in detail in the Appendix. Using this notation for the nonlinear elastic modulus, the balance of forces can be described by the wave equation including viscosity (η) that is based on the Voigt's model (23):

$$\rho \frac{\partial v_y}{\partial t} = E \frac{\partial F}{\partial x} - \eta \frac{\partial^2 F}{\partial x \partial t}, \quad [9]$$

(ρ assigns the material density). If we assume a solution of the form

$$u_y = A_v \exp\left(i\omega t + i\frac{\omega}{c} x - \gamma x\right), \quad [10]$$

($\omega = 2\pi f_v$, $c = \sqrt{E/\rho}$), Eq. [9] yields the damping coefficient as

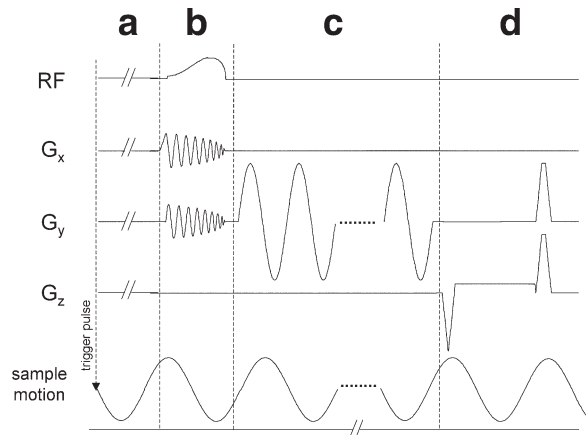


FIG. 3. 1D-gradient echo sequence with a variable number of encoding gradient periods. Additionally, a variable time delay between the oscillation trigger and the beginning of the sequence was introduced to achieve time resolution of the propagating waves. The scheme is drawn for $2f_G = f_v$.

$$\gamma = ik - \omega \sqrt{\frac{\rho}{i\eta\omega - E}} \quad [11]$$

For fitting the experiments, u_y can be calculated numerically starting with the linear elastic modulus $E = \mu$ that bounds $u_y(t = 0, x)$.

MATERIALS AND METHODS

We examined MRE-based detection of nonlinear wave propagation using an agarose gel phantom. The sample was prepared from a heated solution of 2.0% gel in water, and kept refrigerated for 4 weeks. The spatial extension of the phantom was 79 mm in the X -direction. The shear deflection was achieved along the Y' -axis of the actuator system (see Fig. 1). During excitation, 70 cycles at 150 Hz were applied during each TR. The start of the vibrations was triggered by the MR machine. To ensure a sinusoidal motion path of the transducer plate, a setup of two motion-tracking coils was installed as described elsewhere (25). This allowed for an accurate assessment of the presence of harmonics in the actuator itself, which would appear as nonlinear effects in the phantom. A digital oscilloscope was used to detect the voltage induced by mechanical vibrations of the tracking coils. By adjusting the input voltage of the actuator coil, and the surface pressure of the transducer plate on the phantom, we were able to minimize frequencies that were present at frequencies beyond 150 Hz. The maximum deflection amplitude was adjusted with 1 mm peak-to-peak.

1D MRE Sequence

The shear wave displacement was recorded in terms of phase-difference images that displayed one spatial and one time-resolved dimension. This x - t projection was achieved with the use of the motion-sensitive pulse sequence shown in Fig. 3. A 2D radiofrequency (RF) pulse was applied to excite a column along X through the mate-

rial (26). The RF pulse consisted of an eight-loop spiral of approximately 6 ms duration, and was used to excite a column of approximately 2.5 cm in diameter (full width at half maximum). The sinusoidal motion-encoding gradient was applied according to standard MRE techniques. The gradient frequency was varied between 150 and 750 Hz, with period numbers of 2–20. After motion encoding was performed, a gradient echo was acquired while a spatial-encoding gradient was applied parallel to the excited column. Each echo was collected at a bandwidth of approximately ± 15.625 kHz, and was sampled for 256 points over a 24-cm field of view (FOV). The time resolution was achieved by a variable delay inserted between a trigger pulse at the beginning of the sequence and the start of the RF excitation. The mechanical excitation was triggered each TR = 2 s with an incremental progression of phase shift ι . This resulted in a time resolution of $1/8$ of the period length of the motion-encoding gradient. The sequence was implemented on a General Electric Signa LX 1.5-Tesla MR system (GE Medical Systems, Waukesha, WI) with gradient amplitude and slew rates of 40 mT/m and 150 mT/m/ms, respectively. For reconstruction, we applied a 1D-Fourier transform along X , and employed manual phase unwrapping to create a linear representation of particle displacement. We subtracted two 180° -shifted wave images to exclude static phase components of the signal.

MRE Wave Simulations

The appearance of nonlinear MRE wave images is determined by the propagation of nonlinear harmonics, as well as by the details of the motion-encoding gradient. To reproduce this complex correlation, we employed a two-step algorithm as follows:

1. To set up the boundary condition of Eq. [10], we determined the linear shear modulus μ , the displacement amplitude A_v , and the viscosity η by fitting $u_y(t = 0, x)$ to the experimental 150-Hz fundamental vibrations. Then, the nonlinear elastic moduli E_1 and E_2 (Eq. [8]) were synchronously varied, yielding 4D data sets of nonlinear x - t -wave images as a function of both elasticity parameters.

2. We then applied virtual motion encoding to the x - t -wave images to scale all present frequency components with respect to the motion-encoding gradient frequency and the number of applied gradient cycles. To match the length of the virtual motion encoding, the x - t -wave images from step 1 (corresponding to one φ -cycle) were concatenated along the t -dimension.

We processed the experimental and simulated data by applying a 1D Fourier transform along the time axis. The amplitudes of the 4th (600 Hz) and 5th (750 Hz) harmonics were quantitatively evaluated as a function of position. The agreement between the simulations and experimental MRE data was assessed by means of the variance χ (i.e., the mean squared deviation normalized by the experimental error). Data processing and simulations were performed with Matlab 6.5 (The MathWorks Inc.). The computation time for one 128×128 pixel x - t -wave image was approximately 3 s on a Pentium 4, 2.6 GHz PC.

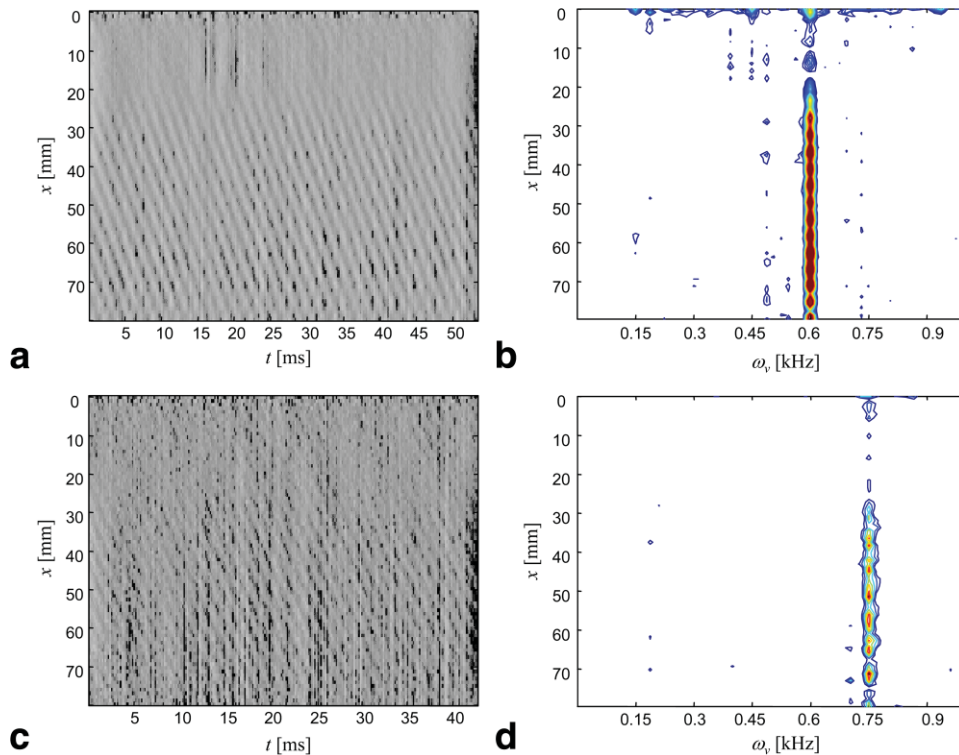


FIG. 4. Experimental x - t -wave images and magnitude spectra of the 4th (a and b) and 5th (c and d) harmonics of 150 Hz fundamental vibrations. In this experiment, $n_G = 20$, i.e., the filter condition was matched corresponding to Eq. [6]. The transducer plate was attached at the upper boundary of the phantom. One can see that nonlinear actuator vibrations induce small vibration intensities in the very upper range. The major intensity growing along X reveals the nonlinear elastic behavior of the phantom. [Color figure can be viewed in the online issue, which is available at www.interscience.wiley.com.]

RESULTS

The MRE x - t data for the 4th and 5th harmonic components at 600 and 750 Hz, and their 1D Fourier transform are demonstrated in Fig. 4. The gradient frequency was set to 600 (a and b) and 750 Hz (c and d), respectively, with a number of gradient periods $n_G = 20$. For this specific number of gradient cycles, both frequencies fulfill the filter condition of Eq. [6] (with $n = 4$ and 5 for $f_v = 750$ and 600 Hz, respectively), so only the motions arising from both selected frequencies are detectable. In contrast, if n_G is changed to 19 periods, off-resonance frequencies appear in the wave image, which are then dominated by the main frequency of 150 Hz (see Fig. 5). In addition to the resonance vibration with $f_G = f_v$, the 1st (150 Hz), 2nd (300 Hz), and 3rd (450 Hz) harmonic oscillations are visible. Their amplitudes obey the relations of Eqs. [3] and [5] depending on the spatial phase θ . The strong fundamental vibrations at 150 Hz in Fig. 5a and c were used to determine the deflection amplitude and wave number. An interactively controlled fit routine based on a sinusoidal function with variable amplitude, frequency, and damping revealed a maximum deflection of $A_v = 0.50 \pm 0.02$ mm, a wavelength of 31.85 ± 0.05 mm for the 150-Hz signal, and a damping coefficient $\gamma = 8.7 \pm 0.2$ m $^{-1}$. On the basis of the wavelength, the shear modulus μ was determined with 23 ± 1 kPa, assuming material homogeneity and a material density of 1 kg/l. The viscosity was determined from the damping coefficient of Eq. [11], with 2.15 ± 0.05 Pa s.

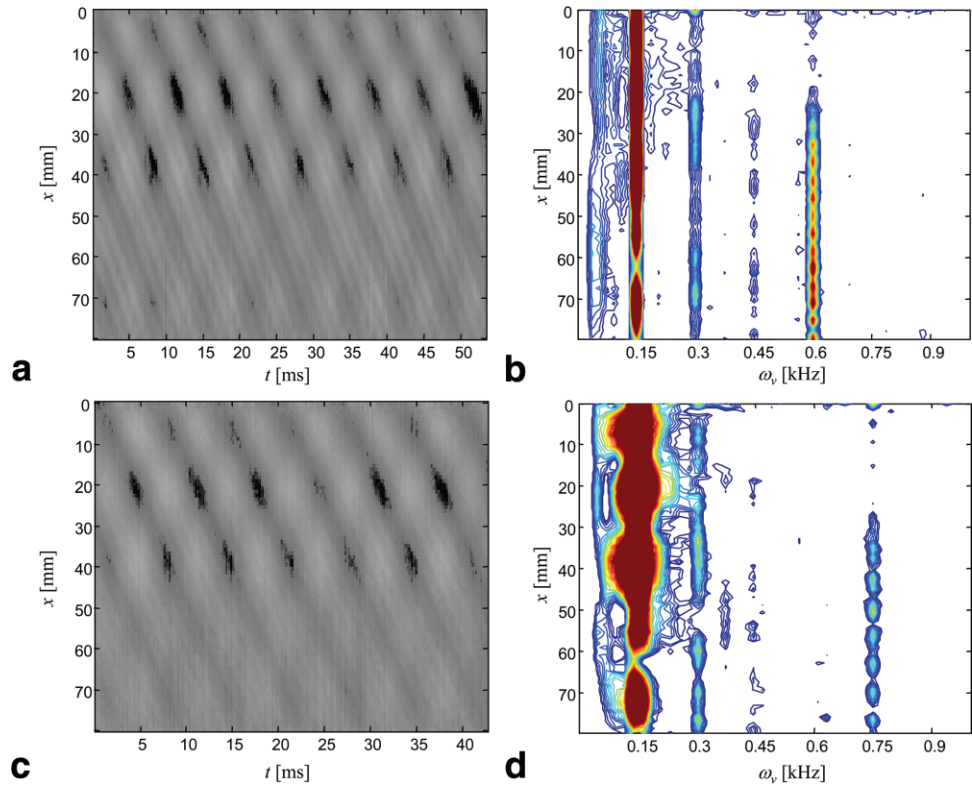
To simulate the material's nonlinear behavior, we considered the experimental intensity profiles of the 4th (600 Hz) and 5th (750 Hz) higher harmonic frequencies along X . Using the correlation of x and y displacement by ζ , we found that with pure transverse shear excitation ($\zeta =$

0) the nonlinear wave propagation generates odd Fourier components, whereas for $\zeta \neq 0$, both odd and even harmonics are superposed.

Figure 6a shows the experimental and simulated amplitude profiles along the object extension for the 4th and 5th higher harmonic vibrations. The experimental profiles at 600 and 750 Hz were obtained from the magnitude spectra shown in Fig. 4b and d. Both amplitude curves are modulated with an oscillating signal that could be removed with a band-gap. The resulting simulated curves are plotted together with both the filtered and unfiltered experimental data. The slope of the profiles shows that in both cases, the amplitude increases with increasing distance to the transducer. With a maximum amplitude of about 3.3 μm , the 4th harmonic shows a threefold higher amplitude than the 5th harmonic, which exhibits a maximum amplitude of approximately 1.1 μm . To calculate the variation χ of the experimental data with respect to the simulated data, we restricted our attention to a spatial range between 20 mm and the phantom boundary (79 mm). To normalize χ , we estimated the experimental errors of ± 0.3 μm (600 Hz) and ± 0.15 μm (750 Hz). Varying E_1 and E_2 allowed us to plot the χ contour to determine its minimum (i.e., the best-fitting combination of these elastic variables). Since the same E_1 - E_2 pair that fits one higher harmonic must fit all other present frequencies, both χ_{600} - and χ_{750} -contours are shown overlaid to estimate the area where the minima of both contours coincide (Fig. 6b). It was found that both minima correlate with $E_1 = 28.5 \pm 1.0$ kPa and $E_2 = 4.5 \pm 0.5$ kPa.

To demonstrate the feasibility of the nonlinear wave simulations, Fig. 7 shows x - t -wave images that correspond to the experiments of Fig. 5. These images were produced

FIG. 5. Experiments corresponding to Fig. 4, but with $n_G = 19$. Here the fundamental vibration dominates the x - t -wave images in the upper half of the phantom, whereas with growing distance to the actuator (upper edge of the images), the higher harmonic frequencies of 600 Hz (a and b) and 750 Hz (c and d) become visible. [Color figure can be viewed in the online issue, which is available at www.interscience.wiley.com.]



with the same experimental parameters of Fig. 5 ($f_G = 0.6$ kHz (a and b), $f_G = 0.75$ kHz (c and d), and $n_G = 19$ (a–d)). The nonlinear elasticity parameters used correspond to the E_1 and E_2 derived in Fig. 6.

DISCUSSION

We have demonstrated that nonlinear MRE allows the observation of higher harmonic vibrations as multiples of the excitation frequency. However, both the nonlinear vibrations of the actuator unit, and the nonlinear elastic

material properties may cause these higher harmonics. In our experiments, a small amplitude fraction was found that showed about 5% of the main vibration (150 Hz) intensity for 300 and 450 Hz (2nd and 3rd harmonics). For higher harmonics of 600 and 750 Hz (4th and 5th harmonics), the vibration amplitude introduced by the mechanical performance of the actuator was further reduced to a negligible amount. For this reason, both 4th and 5th harmonics were selected for further experimental and theoretical examinations. Their intensities became highly visible after Fourier transformation was performed, as shown in the

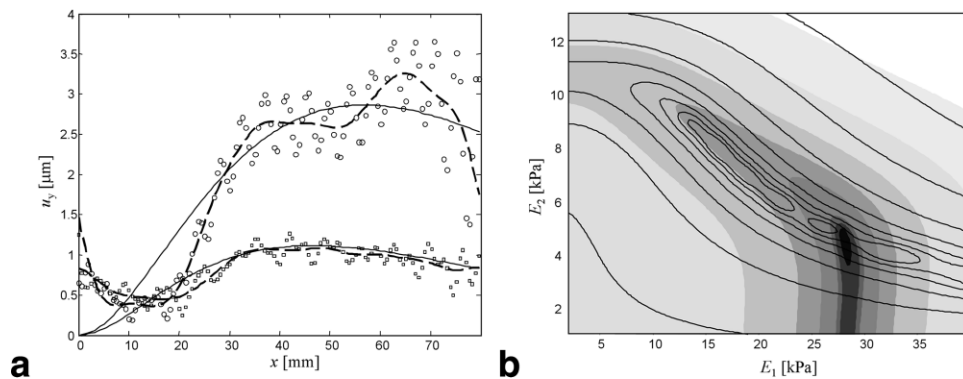


FIG. 6. a: Experimental magnitude amplitudes of 600 Hz (○) and 750 Hz (□) higher harmonic vibrations with Fourier-filtered data (dashed lines). The constant offset of the data may originate from a shallowly varying longitudinal wave that can be introduced by a small rotational component of the actuator motion. The solid lines correspond to the expected amplitudes by minimizing χ (see text). Simulation parameters were chosen using the contour plot in b. b: Contours of χ as a function of the two nonlinear elasticity parameters E_1 and E_2 (Eq. [8]). The open contour patches indicate the quality of the fits of the 600-Hz amplitude curve (χ_{600}), whereas the gray patches show the variance that occurred during the fitting of the 750-Hz profile line (χ_{750}). The isolines belong to $\chi = 0.1 \cdot 2^n$. The coinciding range of minimum standard deviations that corresponds to $E_1 = 28.5 \pm 1.0$ kPa and $E_2 = 4.5 \pm 0.5$ kPa indicates the parameters of the best-fitting simulations.

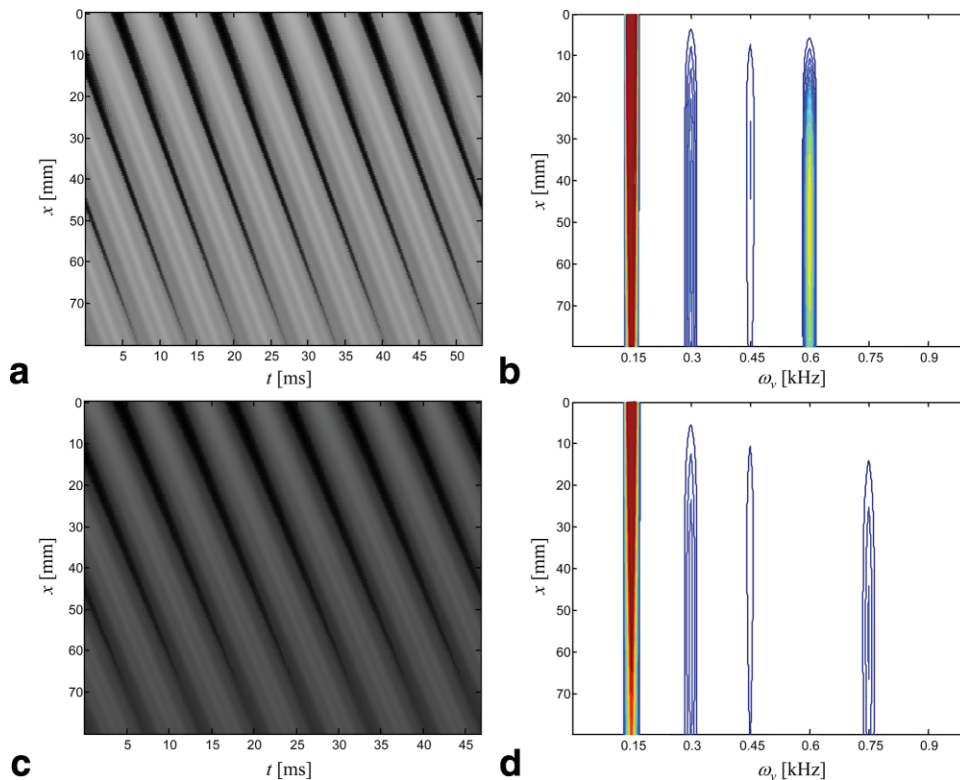


FIG. 7. Simulations of nonlinear wave propagation using the elasticity parameters and relaxation rate deduced from the χ plot of Fig. 6b. The vibration frequency and setup of the virtual motion-encoding gradient correspond to the experimental conditions of Fig. 6 (i.e., $f_v = 0.15$ kHz; $n_G = 19$; $f_G = 0.6$ kHz (a and b) and $f_G = 0.75$ kHz (c and d)). [Color figure can be viewed in the online issue, which is available at www.interscience.wiley.com.]

contour spectra of Fig. 4, where the filter condition (Eq. [6]) is matched. The same information can be obtained for multiple oscillations in a single experiment when n of Eq. [6] is chosen to be a non-integer number. Figure 5 demonstrates how x - t -wave images in nonlinear MRE appear if the filter condition is not fulfilled. To quantitatively evaluate the spectral content of such wave images, a suitable scaling of the encoded amplitudes corresponding to Eq. [3] must be applied for each oscillation. Qualitatively, both Figs. 4 and 5 reveal that the intensity of higher harmonics increases as the wave travels through the object. This observation is consistent with the well-known accumulated effect of harmonic waves through a sample to form a shock wave (20,27). Furthermore, it demonstrates that we observed nonlinear wave propagation due to nonlinear elasticity, as opposed to frequencies introduced by the actuator. This finding is well demonstrated in the spectra of Fig. 4: at the upper boundary of the phantom, a small fraction of intensity emerges that was introduced by the actuator. This higher harmonic vibration disappears after approximately 10 mm for both 600 and 750 Hz. In both cases, the nonlinear mechanism becomes apparent after approximately 20 mm, which results from the nonlinear stress-strain relation of the material. In the range of a 20–30-mm distance to the actuator, both 4th and 5th harmonics reach their maximum values, which bounds the shock distance of the agarose phantom under the applied deflection. Therefore, we neglected the presence of waves from the actuator within a distance of 20 mm in the quantitative evaluation of the nonlinear harmonics.

It has been shown in the literature that pure transverse shear wave excitation results solely in odd-harmonic frequencies (20). However, the experimental observations

(Figs. 4 and 5) show a significant amplitude of the 4th harmonic frequency. Extending the model of pure transverse wave excitation along Y to combined X - Y -wave propagation allows the theoretical prediction of the even harmonic frequencies observed. With this transition to a more complex strain model (see Fig. 1), the number of unknown constitutive parameters increases from one to four. Therefore, the strain parameters were reduced by both the condition of incompressibility and the correlation of $u_x(x,y)$ with $u_y(x,y)$ using the factor ζ . The first assumption is well established for agarose gels and many biological soft tissues. The correlation of $u_x(x,y)$ and $u_y(x,y)$ is justified if a slight tilt of the actuator system with respect to the B_0 -field is taken into account. Such misalignment within a few degrees is on the order of the accuracy of standard electromechanical actuators in MRE. In our simulations, however, we used the correlation factor ζ as an implicit variable of the parameter E_2 , whereas E_1 provided a measure of nonlinear elasticities independently of x deflection components. Thus, while E_2 is important for the explanation of the presence of the 4th-order harmonic, its value is strongly dependent on the geometrical alignment of the experiment, and it is E_1 that represents a “truly” measured (i.e., independent of the geometry) nonlinear parameter.

The data of Fig. 6b show the strategy we used to determine the best-fitting E_1 - E_2 parameter pair. The distinct range in which the minima of the χ_{600} - and χ_{750} -contour overlapped was selected as the best range for fitting the elasticity coefficients E_1 and E_2 . This range of $E_1 = 28.5 \pm 1.0$ kPa, and $E_2 = 4.5 \pm 0.5$ kPa shows that the coefficient E_1 is much greater than E_2 , indicating a small ζ -factor. To estimate the explicit fraction of $u_x(x,y)$ and thus the tilt

angle α , further information about the nonlinear parameters $C_{1,0}$ and $C_{0,2}$ (see Appendix, Eq. [A11]) is required. Values from literature indicate a great variety of nonlinear elasticity components for gel samples (28,29). Furthermore, sensitive chemical and physical parameters, such as the number of cross-links of the specific gel, and the concentration, temperature, and time of deterioration, are crucial for comparing nonlinear stress-strain relations. The direction components of the applied strain must be carefully considered. As shown here, relatively small values of E_2 (4.5 ± 0.5 kPa) create the 4th harmonic, which itself has three times the intensity of the 5th harmonic. To gain more accurate knowledge about the elasticity coefficients used in the strain energy function (Eq. [A6]), one must determine the deflection along X and Y with a spatial resolution in at least two dimensions. However, in in vivo experiments where scan time is an expensive parameter, the proposed model of correlated x - y -displacement amplitudes would allow investigators to focus in nonlinear wave simulations on the 3rd-order modulus E_1 , which is independent of implicit geometrical considerations. This approach could be employed to reveal the nonlinear elastic properties of diffuse changes of tissue (e.g., cirrhotic liver diseases) or pathologic lesions (e.g., breast tumors (30)) whose extensions clearly exceed the shock distance. For potential in vivo applications of nonlinear MRE, high viscosity must be taken into account. The relatively high viscosity of biological tissues causes strongly damped shear waves, and thus higher harmonics, since the 4th and 5th harmonics of 150 Hz fundamental frequency would be damped off within a few millimeters. On the other hand, by applying a lower fundamental frequency (~ 50 Hz) and capturing the 2nd and 3rd harmonics, researchers can observe reasonable signal amplitudes over a pathway that is long enough to allow the waves to accumulate an observable amount of nonlinear properties. In addition, the linear behavior of the actuator must be carefully monitored, since in this frequency range electromechanical actuators may introduce some anharmonic vibrations, as shown in Ref. 25.

CONCLUSIONS

A dynamic 1D MRE technique was used to detect nonlinear wave propagation in agarose. The use of 1D nonlinear MRE experiments allows adequate temporal sampling to be achieved in a reasonable time for clinical applications. The resulting nonlinear wave amplitude profiles along a spatial axis reveal the growing intensity of higher harmonics with propagation through the phantom. While for pure transverse shear wave excitation, the intensity of only the odd-harmonic frequencies was expected, the experiments revealed the existence of even harmonics. A model of correlated displacement components was introduced that bounds a small portion of the transverse wave intensity parallel to the image axis. Using this model, we were able to deduce nonlinear elasticity parameters from the profile curves of the 4th and 5th harmonics. This work demonstrates how MRE can be applied for the observation, analysis, and quantification of nonlinear tissue vibrations.

APPENDIX

Here the nonlinear shear modulus E is deduced with the use of the displacement vector \mathbf{u} (Eq. [7]). The correlated displacements yield the deformation gradient

$$\mathbf{F} = \begin{bmatrix} \zeta \frac{\partial u_y}{\partial x} + 1 & \zeta \frac{\partial u_y}{\partial y} \\ \frac{\partial u_y}{\partial x} & \frac{\partial u_y}{\partial y} + 1 \end{bmatrix}, \quad [\text{A1}]$$

where \mathbf{F} is used to define the left and right Cauchy-Green strain tensors $\mathbf{G}_l = \mathbf{F}\mathbf{F}^T$ and $\mathbf{G}_r = \mathbf{F}^T\mathbf{F}$, respectively. Since in practice α is small (i.e., in the range of $\pm 3^\circ$, yielding a factor ζ of about ± 0.05), quadratic and higher-order terms of ζ can be approximated to be zero. In the following, this assumption is applied to all potentials of $\zeta > 1$. The invariants of \mathbf{G}_l are given with

$$\begin{aligned} I_1 &= \text{trace}(\mathbf{G}_l) \\ I_2 &= \det(\mathbf{G}_l) \cdot \text{trace}(\mathbf{G}_l^{-1}) \\ I_3 &= \det(\mathbf{G}_l). \end{aligned} \quad [\text{A2}]$$

Under the assumption of incompressibility ($I_3 = 1$), the deformation component $\partial u_y / \partial y$ can be derived from Eq. [A2] with two roots:

$$\frac{\partial u_y}{\partial y} = \begin{cases} -\zeta F \\ -\zeta F - 2 \end{cases}, \quad [\text{A3}]$$

where $F = \partial u_y / \partial x$ is the quantity of deformation that describes the 1D strain-wave amplitude measured in 1D nonlinear MRE experiments. Substitution of Eq. [A3] into Eq. [A2] results in two identical invariants of \mathbf{G}_l :

$$I_1 = I_2 = 2 + F^2. \quad [\text{A4}]$$

The elements of the strain tensor $\varepsilon = 1/2(\mathbf{G}_r - \mathbf{I})$ (where \mathbf{I} denotes the tensor identity) are given by

$$\varepsilon = \frac{1}{2} \begin{bmatrix} 2\zeta F + F^2 & F - \zeta F^2 \\ F - \zeta F^2 & -2\zeta F \end{bmatrix}. \quad [\text{A5}]$$

The strain-energy function Φ can be evaluated with the use of a polynomial hyperelastic model (31):

$$\Phi = \sum_{i+j=1}^2 C_{ij}(I_1 - 2)^i(I_2 - 2)^j. \quad [\text{A6}]$$

The first-order term of Φ refers to a Mooney-Rivlin material that leads to a nonlinear stress-strain relationship under uniaxial loading while yielding a linear elasticity for pure transverse shear strain. Since the latter was the main displacement component of the nonlinear experiments, a 2nd-order polynomial form is used henceforth, yielding a nonlinear stress-strain relation for pure transverse shear strain.

The strain-energy function allows the second Piola-Kirchhoff stress tensor to be derived:

$$\mathbf{T} = \frac{\partial \Phi}{\partial \boldsymbol{\varepsilon}} - p\mathbf{I}. \quad [\text{A7}]$$

Here, p represents the hydrostatic pressure that is introduced to fulfill incompressibility constraints. The derivative of the strain-energy function with respect to the strain tensor elements of $\boldsymbol{\varepsilon}$ can be expressed in terms of the invariants of \mathbf{G}_1 using

$$\mathbf{T} = 2 \left[\left(\frac{\partial \Phi}{\partial I_1} + I_1 \frac{\partial \Phi}{\partial I_2} \right) \mathbf{G}_1 - \frac{\partial \Phi}{\partial I_2} \mathbf{G}_1^2 \right] - p\mathbf{I}, \quad [\text{A8}]$$

which still holds for an incompressible material. The elastic modulus E is obtained by deriving the elements of \mathbf{T} with respect to the deformation tensor. Using the first root of Eq. [A3] to substitute $\partial u_y / \partial y$, the following equation of motion can be obtained as

$$\frac{\partial F}{\partial x} E = \frac{dT_{xy}}{dF} \frac{\partial F}{\partial x} - \zeta \frac{dT_{yy}}{dF} \frac{\partial F}{\partial x}. \quad [\text{A9}]$$

E can be derived as given in Eq. [8] using the following notation:

$$\begin{aligned} E_1 &= 2(C_{1,1} + 2C_{2,0}) \\ E_2 &= \zeta[E_1 + 2(C_{1,1} + 2C_{0,2})] \\ \mu &= 2C_{1,0}. \end{aligned} \quad [\text{A10}]$$

REFERENCES

- Dresner MA, Rossman PJ, Kruse SA, Ehman RL. MR elastography of the prostate. In: Proceedings of the 10th Annual Meeting of ISMRM, Philadelphia, 1999. p 526.
- Sinkus R, Nisius T, Lorenzen J, Kemper J, Dargatz M. In-vivo prostate MR-elastography. In: Proceedings of the 11th Annual Meeting of ISMRM, Toronto, Canada. 2003. p 586.
- Felmlee JP, Rossman PJ, Muthupillai R, Manduca A, Dutt V, Ehman RL. Magnetic resonance elastography of the brain. In: Proceedings of the 5th Annual Meeting of ISMRM, Vancouver, Canada. 1997. p 683.
- Kruse SA, Dresner MA, Rossman PJ, Felmlee JP, Jack CR, Ehman RL. Palpation of the brain using magnetic resonance elastography. In: Proceedings of the 7th Annual Meeting of ISMRM, Philadelphia, 1999. p 258.
- Rydberg J, Grimm R, Kruse SA, Felmlee JP, McCracken P, Ehman RL. Fast spin-echo magnetic resonance elastography of the brain. In: Proceedings of the 9th Annual Meeting of ISMRM, Glasgow, Scotland, 2001. p 1647.
- Braun J, Bernarding J, Tolxdorff T, Sack I. In vivo magnetic resonance elastography of the human brain using ultrafast acquisition techniques. In: Proceedings of the 10th Annual Meeting of ISMRM, Honolulu, 2002. p 2597.
- Dresner MA, Rose GH, Rossman PJ, Muthupillai R, Manduca A, Ehman RL. Magnetic resonance elastography of skeletal muscle. *J Magn Reson Imaging* 2001;13:269-276.
- Sack I, Bernarding J, Braun J. Analysis of wave patterns in MR elastography of skeletal muscle using coupled harmonic oscillator simulations. *Magn Reson Imaging* 2002;20:95-104.
- Uffman K, Mateiesi S, Quick HH, Ladd ME. In vivo determination of biceps elasticity with MR elastography. In: Proceedings of the 10th Annual Meeting of ISMRM, Honolulu, 2002. p 37.
- Lawrence AJ, Rossman PJ, Mahowald JL, Manduca A, Hartmann LC, Ehman RL. Assessment of breast cancer by magnetic resonance elastography. In: Proceedings of the 7th Annual Meeting of ISMRM, Philadelphia, 1999. p 525.
- Sinkus R, Lorenzen J, Schrader D, Lorenzen M, Dargatz M, Holz D. High-resolution tensor MR elastography for breast tumour detection. *Phys Med Biol* 2000;45:1649-1664.
- Van Houten EE, Doyley MM, Kennedy FE, Weaver JB, Paulsen KD. Initial in vivo experience with steady-state subzone-based MR elastography of the human breast. *J Magn Reson Imaging* 2003;17:72-85.
- Muthupillai R, Lomas DJ, Rossman PJ, Greenleaf JF, Manduca A, Ehman RL. Magnetic resonance elastography by direct visualization of propagating acoustic strain waves. *Science* 1995;269:1854-1857.
- Knutsson H, Westin CJ, Granlund G. Local multiscale frequency and bandwidth estimation. In: Proceedings of the IEEE International Conference on Image Processing, Austin, 1994. p 36-40.
- Manduca A, Muthupillai R, Rossman PJ, Greenleaf JF, Ehman RL. Image processing for magnetic resonance elastography. In: Proceedings of the SPIE International Symposium on Medical Imaging, San Diego, 1996. p 616-623.
- Oliphant TE, Manduca A, Ehman RL, Greenleaf JF. Complex-valued stiffness reconstruction for magnetic resonance elastography by algebraic inversion of the differential equation. *Magn Reson Med* 2001;45:299-310.
- Van Houten EE, Paulsen KD, Miga MI, Kennedy FE, Weaver JB. An overlapping subzone technique for MR-based elastic property reconstruction. *Magn Reson Med* 1999;42:779-786.
- Braun J, Buntkowsky G, Bernarding J, Tolxdorff T, Sack I. Simulation and analysis of magnetic resonance elastography wave images using coupled harmonic oscillators and Gaussian local frequency estimation. *Magn Reson Imaging* 2001;19:703-713.
- Catheline S, Gennisson J-L, Chaffai S, Fink M. Measuring non-linear parameters of soft solids using transient elastography. In: Proceedings of the 1st International Conference on the Ultrasonic Measurement and Imaging of Tissue Elasticity, Niagara Falls, 2002.
- Catheline S, Gennisson JL, Tanter M, Fink M. Observation of shock transverse waves in elastic media. *Phys Rev Lett* 2003;91:164301.
- Catheline S, Gennisson JL, Fink M. Measurement of elastic nonlinearity of soft solid with transient elastography. *J Acoust Soc Am* 2003;114(6 Pt 1):3087-3091.
- Lee-Bapty IP, Crighton DG. Nonlinear wave motion governed by the modified Burgers equation. *Phil Trans R Soc Lond A* 1987;323:173-209.
- Fung Y. *Biomechanics: mechanical properties of living tissue*. New York: Springer-Verlag; 1993.
- Glaser KJ, Felmlee JP, Ehman RL. Rapid shear stiffness estimations using 2-D spatial excitations in magnetic resonance elastography. In: Proceedings of the 10th Annual Meeting of ISMRM, Honolulu, 2002. p 39.
- Plewes DB, Luginbhuh C, McGowan C, Sack I. An inductive method to measure mechanical excitation spectra for MRI elastography. *Concepts Magn Reson B: Magn Reson Eng* 2004;21B:32-39.
- Hardy CJ, Cline HE. Broadband nuclear magnetic resonance pulses with two-dimensional spatial selectivity. *J Appl Phys* 1989;66:1513-1516.
- Bedford A, Drumheller DS. *Introduction to elastic wave propagation*. West Sussex: John Wiley & Sons; 1994.
- Bot A, van Amerongen I, Groot R, Hoekstra N, Agterof W. Large deformation rheology of gelatin gels. *Polym Gels Netw* 1996;4:189-227.
- Tang J, Tung M, Lelievre J, Zeng Y. Stress-strain relationships for gellan gels in tension, compression and torsion. *J Food Eng* 1997;31:511-529.
- Sinkus R, Weiss S, Wigger E, Lorenzen J, Dargatz M, Kuhl C. Non-linear elastic tissue properties of the breast measured by MR-elastography—initial in-vitro and in-vivo results. In: Proceedings of the 10th Annual Meeting of ISMRM, Honolulu, 2002. p 33.
- Chernykh KF. *An introduction to modern anisotropic elasticity*. New York: Begell House Inc.; 1997.